Dovepress
Taylor & Francis Group

Open Access Full Text Article

ORIGINAL RESEARCH

Photothermal Antibacterial Effect of Gold Nanostars Coating on Titanium Implant and Its Osteogenic Performance

Li Li[1,]*, Jiayao Wu[1,]*, Linru Liu[2], Pei Zhang[1], Yilin Zhang[2], Zixin Zhou[1], Xu Gao[1], Shengjun Sun[1]

[1]Department of Prosthodontics, School and Hospital of Stomatology, Cheeloo College of Medicine, Shandong University & Shandong Key Laboratory of Oral Tissue Regeneration & Shandong Engineering Research Center of Dental Materials and Oral Tissue Regeneration & Shandong Provincial Clinical Research Center for Oral Diseases, Jinan, Shandong, 250012, People's Republic of China; [2]Shandong Provincial Hospital Affiliated to Shandong First Medical University, Jinan, Shandong, 250021, People's Republic of China

*These authors contributed equally to this work

Correspondence: Shengjun Sun, Email sunshengjun@sdu.edu.cn

Introduction: Titanium implants are widely used in dentistry due to their mechanical strength and biocompatibility, yet their biological inertness and lack of antimicrobial properties contribute to high failure rates from poor osseointegration and infections like peri-implantitis. To address these limitations, this study developed a gold nanostar (GNS)-coated titanium implant (Ti-GNS) and systematically evaluated its osteogenic and photothermal antibacterial functions. The research aimed to enhance osseointegration through surface modification while leveraging GNS's photothermal effect for on-demand antibacterial activity, offering a dual-functional strategy to improve implant performance.

Methods: GNSs were synthesized and anchored onto titanium surfaces through surface modification via silanization. Material characterization included morphological, elemental, and photothermal analyses. In vitro experiments assessed osteogenic differentiation of bone marrow stem cells (ALP activity, mineralization, gene/protein expression) and antibacterial efficacy against *Staphylococcus aureus* and *Escherichia coli* under NIR. In vivo performance was evaluated by implanting Ti, Ti-Si (silanized), and Ti-GNS in rat femurs, followed by micro-CT and histological analysis.

Results: Silanization and GNS deposition optimized titanium surfaces by significantly enhancing wettability and nanoscale roughness, while photothermal activation under NIR irradiation demonstrated temperature-dependent responsiveness. Furthermore, in vivo evaluations confirmed Ti-GNS biocompatibility and revealed enhanced osteogenic potential through promoted cell adhesion, proliferation, as well as osteoinductive marker expression. Notably, the Ti-GNS group exhibited superior osseointegration alongside stable antimicrobial efficacy post-NIR exposure.

Conclusion: GNS-coated titanium implants synergistically enhance osteogenesis and provide NIR-responsive antibacterial activity. The modified surface improved cell interactions and bone formation while achieving near-complete bacterial elimination under light activation. This dual-functional strategy addresses key challenges in implantology, though long-term stability and clinical translation require further investigation. The study establishes a foundation for photothermal antimicrobial implants with significant potential in dental applications.

Keywords: gold nanostars, peri-implantitis, osteoinduction, surface modification

Introduction

Titanium and its alloys are widely recognized in dental implants due to their exceptional mechanical properties, biocompatibility, osseointegration capacity, and high corrosion resistance.[1–4] Nonetheless, clinical applications of titanium implants face several significant challenges.[5] One prominent issue is that the integration rate between the implant and host bone often falls short of clinical expectations. Furthermore, titanium implants lack adequate antimicrobial properties, rendering them vulnerable to bacterial infections and complications, such as peri-implantitis (PI),

Graphical Abstract
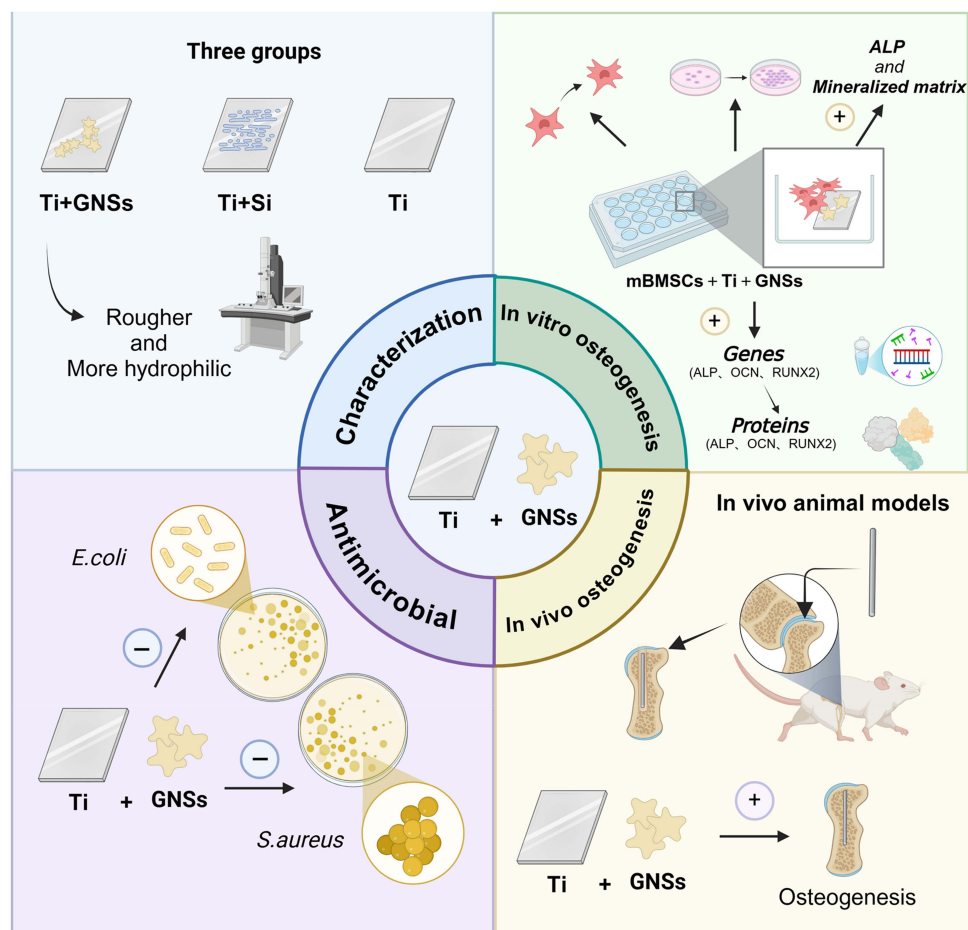
which can ultimately result in implant failure.[6–8] The prevalence of implant-related infections, including PI, has risen in conjunction with the broader adoption of implant technology.[9,10] In natural state, titanium surfaces are frequently enveloped by a biologically inert titanium dioxide film, which impedes cell adhesion and colonization, thereby adversely affecting the osseointegration process. As a result, enhancing the osseointegration capacity of titanium implants through surface modifications, while simultaneously imparting antimicrobial properties, has become a pivotal area of contemporary research. Researchers are investigating various surface modification techniques aimed at improving osseointegration and mitigating implant-related infections.[1–13] One promising approach involves the development of antimicrobial coatings to inhibit bacterial adhesion, utilize contact-based sterilization, or employ photocontrolled sterilization. In particular, photothermal antimicrobial strategies have attracted considerable interest due to their benefits, which include avoiding the introduction of exogenous metal ions (as bactericidal effects are achieved through localized hyperthermia-induced physical disruption of bacterial membranes and protein denaturation, rather than chemical ion release), minimizing the risk of drug resistance (due to the non-specific thermal damage mechanism that prevents bacterial adaptive evolution), and offering broad-spectrum antimicrobial efficacy (effective against both Gram-positive and Gram-negative strains via temperature-mediated structural destruction).[14–17] Photothermal antimicrobial therapy specifically involves the application of light sources, especially near-infrared (NIR) irradiation, to activate photosensitizers (PTAs). These PTAs convert light energy into heat, resulting in localized temperature increases that lead to protein denaturation and irreversible bacterial destruction, thereby achieving sterilization. Within this context, photosensitizers play a crucial

role by facilitating light-to-heat conversion, with nanomaterials such as metal nanoparticles and metal oxides being among the most favored options.[18,19]

Gold nanoparticles (GNPs), a class of precious metal nanomaterials, have found extensive applications in nanomedicine, particularly in photothermal therapy for cancer and antimicrobial treatments. Recent advancements have enabled the synthesis of GNPs in various morphologies, including spherical, rod-shaped, and star-shaped forms. The structural, magnetic, optical, and electronic properties of these differently shaped GNPs differ from those of simple spherical gold nanoparticles. Gold nanostars (GNSs), characterized by their high anisotropy, feature a central core with multiple sharp tips and possess diameters ranging from 50 to 100 nm. Their unique star-shaped structure significantly enhances their specific surface area, while the core-tip configuration results in two plasmon resonance peaks, optimizing light energy utilization and conversion efficiency. GNSs are widely employed in medical diagnostics, bio-imaging, and, more recently, in photothermal antimicrobial applications, which are particularly relevant to improving dental implant outcomes.[20] In vitro studies have shown that various forms of GNPs, including spherical and rod-shaped particles, can promote osteogenic differentiation and mineralization.[21,22] As a specific subset of GNPs, the ability of GNSs to enhance osteogenesis has garnered increasing interest.[23]

The objective of this study was to fabricate gold nanostar-modified titanium surfaces and to systematically investigate their potential to enhance osteogenic differentiation in vitro. Furthermore, this study aimed to evaluate the antimicrobial effects of gold nanostar-modified titanium surfaces under near-infrared (NIR) irradiation, presenting a novel approach to improving implant osseointegration and offering a photothermal antimicrobial treatment strategy for peri-implantitis.

Materials and Methods

Synthesis of Ti-Gold Nanostars (Ti-GNS)

The fabrication of gold nanostars (GNSs)-coated titanium (Ti-GNS) involved sequential surface modifications. Titanium sheets were mechanically polished using 320-grit, 400-grit, 600-grit, and 1000-grit sandpapers until the surface roughness reaches 0.2–0.4 μm to enhance coating adhesion, ultrasonically cleaned with organic solvents, and treated with UV-ozone to generate hydroxyl groups. Silanization was performed by immersing Ti in a solution containing trimethoxysilane under 70°C for 2 h to form thiol-functionalized surfaces (Ti-Si). GNSs were synthesized via chemical reduction using chloroauric acid and HEPES buffer (pH 7.4) at 30°C for 1 h, followed by centrifugation and resuspension. The silanized Ti was then immersed in the GNSs solution, ultrasonicated, and incubated overnight at 37°C to achieve covalent bonding via Au-S interactions. Surface characterization confirmed successful GNSs immobilization. Through the aforementioned procedures, three experimental groups were established: 1. Ti-GNS group (gold nanostar-coated surface), 2. Ti-Si group (silanized surface), and 3. Ti group (only polishing and cleaning were performed on titanium).

Characterization of Gold Nanostars

The morphology of the titanium sheets post-gold nanostar synthesis was characterized using Transmission Electron Microscopy (TEM). Scanning Electron Microscopy (SEM) was employed to analyze the surface topography of the samples, while Energy-Dispersive X-ray Spectroscopy (EDS) was utilized for point-scan elemental analysis, ensuring precise determination of the elemental composition at selected surface locations. A contact angle goniometer measured the contact angles of three sample groups (Ti-GNS, Ti-SH, Ti). Variations in contact angle were assessed to evaluate the hydrophilicity changes among the three sample groups. Atomic Force Microscopy (AFM) was employed to further examine surface morphology, with surface roughness (Rq values) measured using a Surface Profilometer; the average of these measurements was reported as the surface roughness parameter. X-ray Photoelectron Spectroscopy (XPS) was applied to investigate the elemental composition and distribution of valence states on the surfaces of the different sample groups. Finally, photothermal performance testing was conducted by placing the titanium sheets in a 24-well cell culture plate, each well containing 1 mL of culture medium. The plate was pre-incubated at 37°C for 2 hours before being irradiated with an 808 nm near-infrared (NIR) laser at an intensity of 0.5 W/cm². Surface temperature changes were

monitored in real-time using an infrared thermal camera, with temperature data recorded every minute to plot the relationship between surface temperature and irradiation duration.

Cell Culture

Murine bone marrow-derived mesenchymal stem cells (mBMSCs) were isolated from 4-week-old male C57BL/6 mice. Mice were sacrificed by cervical dislocation and fully immersed in 75% ethanol for 15 minutes for disinfection. Under sterile conditions, the bilateral femurs and tibias were excised and cleaned of residual muscle tissue. Both ends of the long bones were trimmed to allow complete flushing of the marrow cavity with sterile PBS. The bone marrow was flushed into pre-prepared α-MEM culture medium supplemented with 10% fetal bovine serum until the bones appeared completely white. After centrifugation at 1000 rpm for 5 minutes and discarding the supernatant, the cells were resuspended in the culture medium, dissociated by repeated pipetting, and seeded into culture flasks. Cells were incubated in a humidified 37°C incubator with 5% CO_2 for 48 hours without disturbance. The culture medium was refreshed on day 3, and cell morphology and adhesion were observed. Upon reaching approximately 80% confluence, cells were harvested using trypsin, passaged at a ratio of 1:3 to 1:4, and early-passage cells were cryopreserved at −80°C for future use.

For experiments, cells from passages 2–4 in optimal growth conditions were selected, digested with 0.25% trypsin, centrifuged, resuspended in α-MEM medium containing 10% fetal bovine serum, and prepared as cell suspensions for further experiments.

Alkaline Phosphatase (ALP) Staining and ALP Activity Assay

The cell suspension prepared previously was added dropwise onto the surface of titanium sheets at an inoculum concentration of 0.5×10^4 cells/mL per well and placed in a 37°C, 5% CO_2 incubator. Two days after cell inoculation, the original culture medium was discarded, and the cells were cultured in osteogenic induction medium (α-MEM medium containing 10% fetal bovine serum, 10 mm sodium β-glycerophosphate, 0.1 μM dexamethasone, and 0.2 mm vitamin C). The osteogenic induction medium was refreshed every other day. The culture was terminated on days 7 and 14, respectively, and alkaline phosphatase activity was quantified using an alkaline phosphatase assay kit and a BCA protein concentration assay kit.

Cell Activity Staining

The prepared cell suspension was carefully added dropwise onto the surface of titanium sheets at an inoculation concentration of 0.3×10^4 cells/mL per well. After incubating for 24 hours at 37°C with 5% CO_2, cell activity on the surface of the material was assessed using the fluorescein diacetate/propidium iodide (FDA/PI) double-staining method.

Cell Proliferation Assay

BMSCs were detached from the culture dishes and seeded onto various types of Ti disks at a density of 5×10^4 cells/mL. Cell proliferation on the surface of the Ti disks was evaluated using a Cell Counting Kit-8 (CCK-8) after 1, 3, and 7 days of culture. At each predetermined time point, the culture medium was replaced with fresh medium containing CCK-8, followed by incubation for 2 hours. Absorbance was then measured at 450 nm using a microplate reader. Additionally, cytotoxicity was assessed using a live/dead cell viability assay kit after 24 and 48 hours of culture. The absorbance values at 450 nm for each group were measured with a microplate reader, and the relative cell proliferation in each group at each time point was calculated.

Alizarin Red S (ARS) Staining and Calcium Deposition Assay

Calcium deposition was quantified using Alizarin Red S and cetylpyridinium chloride staining, following the same plating protocol. Cetylpyridinium chloride was dissolved in a 10 mm sodium phosphate buffer to prepare a 10% mineralized nodule elution solution. A volume of 500 μL of this solution was added to each well. After shaking and incubating at room temperature for 30 minutes, 100 μL of the elution solution from each well was transferred to a 96-well plate. The optical density (OD) was then measured at 620 nm using a spectrophotometer.

Quantitative Real-Time Polymerase Chain Reaction (qRT-PCR)

QRT-PCR was employed to quantify the expression of four genes associated with osteogenesis and osteoclastogenesis in osteoblasts: alkaline phosphatase (ALP), osteocalcin (OCN), osteopontin (OPN), and Runt-related transcription factor 2 (RUNX2). Gene sequences are shown in Table 1.

Western Blotting Analysis

Cell suspensions were seeded dropwise onto the surface of titanium sheets at a density of 1×10^4 cells/mL per well, followed by incubation at 37°C in a 5% CO_2 environment. After 14 days of osteogenic induction, the culture was terminated. The relative expression levels of osteogenic markers, ALP and Runt-related transcription factor 2 (RUNX2), were quantified via Western blot analysis.

In Vivo Animal Test

The animal experiments were approved by the Ethics Committee of the Stomatological Hospital of Shandong University (approval number: 20221012), and all experimental operations met the requirements of the Ethics Committee of Shandong University. This experiment adhered to the "3R" principles (Replacement, Reduction, Refinement) in animal use.

Thirty 6-week-old male Sprague-Dawley (SD) rats were randomly assigned to three groups: the Ti implant group, the Ti-Si implant group, and the Ti-GNS implant group, with 10 rats in each group. A longitudinal incision was made along the skin surface in the knee joint area, followed by blunt dissection of the subcutaneous tissue and muscles to expose the joint structure. The femur was stabilized, and an implant socket was prepared by applying pressure in the center of the joint capsule toward the medullary cavity using a drill under continuous irrigation with pre-cooled normal saline. A titanium rod was implanted, ensuring adequate initial stability. The wound was sutured tightly in layers, followed by cleaning with iodophor and intraperitoneal injection of 0.1 mL of antibiotics. The rats were group-housed according to their respective experimental groups. Three days post-operation, the rat wounds were disinfected with iodophor, monitored for healing, and antibiotics were administered. After three days, the animals were returned to routine care. Subsequent assessments included micro-CT scanning, 3D reconstruction, bone histomorphometric analysis, and hematoxylin and eosin (HE) staining of hard tissue sections.

In vitro Antibacterial Performance Study

Staphylococcus aureus, a common Gram-positive bacterium in the oral cavity, and *Escherichia coli*, a Gram-negative bacterium, were selected as experimental models. The bacterial concentration was adjusted to 1×10^6 CFU/mL, and 1 mL of the bacterial suspension was pipetted onto the surface of each titanium disc. The experiment included two conditions: light exposure and darkness. An 808 nm wavelength diode laser (0.5 W/cm²) served as the light source for irradiating the titanium samples in the light-exposure group. For the irradiation group, the samples were exposed to an 808 nm laser diode (power density: 0.5 W/cm²) for 10 minutes, with real-time thermal monitoring to ensure the temperature remained ≤50°C. The dark group received no irradiation and was further cultured for 12 hours under

Table 1 qRT-PCR Gene and Primer Sequence

Gene	Primer Sequence
GAPDH	Forward:5'-AACTTTGGCATTGTGGAAGG-3'
	Reverse:5'-ACACATTGGGGGTAGGAACA-3'
ALP	Forward:5'-GACTGGTACTCGGATAACGAGA-3'
	Reverse:5'-CTCATGATGTCCGTGGTCAATC-3'
OCN	Forward:5'-GCCCAGACCTAGCAGACACCAT-3'
	Reverse:5'-TTCACTACCTTATTGCCCTCC-3'
RUNX2	Forward:5'-AACTTTGGCATTGTGGAAGG-3'
	Reverse:5'-ACTTGTGGCTCTGATGTTCC-3'

standard conditions. Collecting bacteria from the material surface, performing serial dilution and plate culturing, followed by calculating the antibacterial rate by comparing colony counts between dark and NIR-treated groups. Fluorescence staining and ImageJ analysis were used to quantify live (green) and dead (red) cells, providing dual validation of the material's antibacterial efficacy through colony enumeration and live/dead cell ratios.

After each antibacterial test, titanium samples were ultrasonically cleaned and sterilized, with the procedure repeated. Each bacterial group was cultured on material surfaces for 12 h, and the bacterial inhibition rate was recorded to evaluate antimicrobial stability.

Statistical Analysis

Data are presented as mean ± standard deviation ($\bar{x} \pm SD$). Statistical analyses were conducted using SPSS version 22.0 (IBM SPSS, USA) for data processing, and GraphPad Prism version 5 was utilized for graphical representation. Group differences were evaluated using one-way analysis of variance (ANOVA), followed by Student-Newman-Keuls (SNK) post hoc tests. Statistical significance was defined at p-values of $*p < 0.05$ and $**p < 0.01$.

Results

Characterization of Ti–GNP

TEM

The morphological characteristics of the synthesized GNSs observed under a TEM are presented in Figure 1A. In the low-magnification field of view (a), the synthesized product exhibits relatively good monodispersity, with minimal evidence of particle aggregation or clustering. At higher magnification (b), the GNSs are seen to consist of a central spherical core with multiple tip structures of varying lengths extending outward, and they exhibit a diameter range of 50–100 nm.

SEM

Figure 1B presents the surface micro-morphology of titanium sheets in each group following different surface treatments. The untreated Ti group (a, b) shows a relatively smooth surface. In contrast, the Ti-Si group (c, d) exhibits a marked increase in surface roughness, with the appearance of flake-like structures. Additionally, in the Ti-GNS group (e, f), a uniform layer of deposited GNS is observed, as indicated by the red circles, alongside the aforementioned surface roughness changes.

EDS

Figure 1C presents the energy-dispersive X-ray spectroscopy (EDS) element mapping results of the titanium sheet surfaces after different surface treatments. EDS analysis of the Ti group (a) revealed no detectable silicon (Si) or gold (Au) elements. In the Ti-Si group (b), the presence of Si elements confirms the successful introduction of silicon onto the material surface through silanization. In addition to Si, the Ti-GNS group (c) also shows the appearance of Au elements, demonstrating that the GNSs were successfully anchored to the surface of the titanium sheets.

Contact Angle

Figure 1D presents the contact angle measurements for each group: Ti group (a) exhibited a contact angle of 80.39° ± 0.34, Ti-Si group (b) demonstrated a contact angle of 69.56° ± 0.56, and Ti-GNS group (c) showed a markedly lower contact angle of 33.33° ± 0.17. The high contact angle of nearly 80° on the pure titanium surface indicates its poor hydrophilicity. The slight reduction in contact angle after silanization treatment suggests an improvement in surface wettability, while the significant decrease following the attachment of GNSs demonstrates that the GNS-modified titanium surface exhibits greatly enhanced hydrophilicity.

AFM

Figure 1E presents the surface roughness measurements of the titanium sheets in each group after undergoing different surface treatments. The Rq value, representing the root-mean-square of the height deviations from the central plane within the measured area, is a commonly used parameter for characterizing surface roughness. A higher Rq value
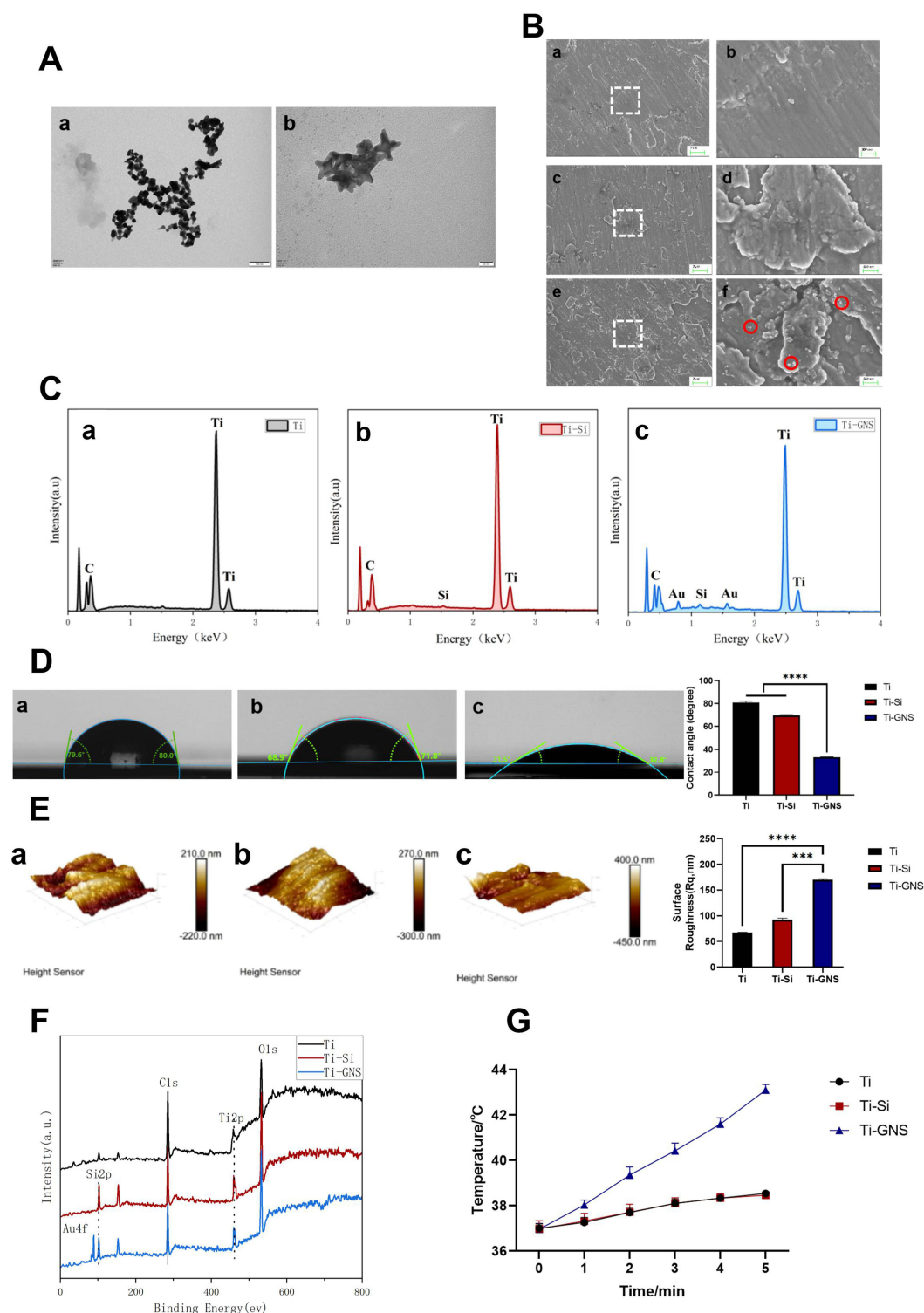
Figure 1 Characterization of Ti, Ti-Si, and Ti-GNS samples. (**A**) Transmission electron microscopy (TEM) images of GNS: low magnification (a) and high magnification (b). (**B**) Scanning electron microscopy (SEM) images of different samples: Ti (a and b), Ti-Si (c and d), Ti-GNS (e and f). The red circles highlight the presence of GNS. (**C**) Energy-dispersive X-ray spectroscopy (EDS) analysis: The EDS analysis of the Ti group (a) shows no detectable silicon (Si) or gold (Au) elements. In contrast, the Ti-Si group (b) indicates successful silanization, while Au and Si elements are detected on the surface of the Ti-GNS group (c). (**D**) Contact angle measurements for the three groups: Ti (a), Ti-Si (b), Ti-GNS (c), along with a statistical comparison of contact angles (d). (**E**) Surface roughness analysis of each group: Ti (a), Ti-Si (b), Ti-GNS (c), and statistical Rq values for the three groups (d). (**F**) X-ray photoelectron spectroscopy (XPS) analysis of elemental valence states on the surfaces of the different groups: Si2p peaks are observed in the Ti-Si and Ti-GNS groups, while Au4f peaks are evident in the Ti-GNS group. (**G**) Surface photothermal performance for each group. Statistical significance was determined: ***$p < 0.005$, ****$p<0.0001$ compared to the Ti or Ti-Si group, n = 5.

indicates a rougher surface. The data show that all surface treatment methods increased the surface roughness of the titanium sheets, which is consistent with the results observed in the SEM analysis.

XPS

Figure 1F illustrates the characterization results of elemental valence states on the surface of titanium sheets from each group after undergoing different surface treatments. The Si2p signal is detectable in both the Ti-Si and Ti-GNS groups following silanization, confirming the successful attachment of silane to the titanium surface. Additionally, the presence of Au4f in the Ti-GNS group further verifies the successful binding of GNS to the titanium surface.

Photothermal Experiment

In Figure 1G, due to the absence of light-responsive materials on the surfaces of the Ti and Ti-Si groups, the temperature increase is minimal and quickly stabilizes under NIR irradiation. However, in the Ti-GNS group, the presence of GNSs results in a significant temperature rise within a short period, demonstrating the photothermal effect of GNSs. This finding provides foundational support for subsequent photothermal antibacterial experiments.

Cellular Morphology

After 24 hours of cell seeding and culture, the cells were stained with Phalloidin and DAPI to visualize the cytoskeleton and nuclei, respectively, on the titanium sheet surfaces. To achieve optimal observation of individual cells, the seeding density was intentionally reduced, ensuring sufficient space for cell extension. As shown in Figure 2A, the cell morphology across all three titanium sheet groups appeared normal, with well-organized actin cytoskeletons. Notably, the Ti-GNS group exhibited a marked increase in the formation of pseudopodia compared to the other two groups, indicating enhanced biocompatibility of the Ti-GNS surface, consistent with the results of material characterization.

Cell Activity Staining

Cells were seeded and cultured for 24 hours, followed by dual staining with FDA/PI (fluorescein diacetate/propidium iodide) to assess cell proliferation on the material surface using fluorescence microscopy. After staining, viable cells fluoresced green, while non-viable cells appeared red. As shown in Figure 2B, all groups exhibited significant cell proliferation. The differences in cell numbers between groups were statistically significant, with the Ti-GNS group demonstrating a markedly higher proliferation rate compared to the other two groups.

Cell Proliferation Assay

After cell seeding on the titanium sheet surfaces, the culture was terminated at 1, 3, and 7 days, and cell proliferation was assessed using the CCK-8 assay. As shown in Figure 2C the overall cell proliferation ability increased progressively over the 1, 3, and 7 days, indicating that the material is non-toxic to cells. Furthermore, at each time point, cell proliferation on the Ti-GNS implant surface showed significant differences compared to the Ti group, aligning with the results of viability staining. The Ti-GNS group demonstrated higher cell proliferation than the other two groups.

ALP

Cells were seeded onto titanium sheets from each group, and the culture was terminated after 7 and 14 days of osteogenic induction. ALP activity was measured in the cells on each material surface at these time points using an ALP assay kit. The results, as shown in Figure 2D indicate that after 7 and 14 days of osteogenic culture, ALP activity in the cells on the Ti-GNS surface was significantly higher than that in the other two groups, with statistically significant differences observed. This finding suggests that the Ti-GNS group effectively enhances the production of ALP.

ARS

Similar to the previously described culturing process, the cells were harvested after 14 and 21 days of osteogenic induction. Alizarin Red staining was used to visualize extracellular mineralized nodules, and cetylpyridinium chloride was employed to prepare the eluent for semi-quantitative analysis of the extracellular mineralized matrix. The eluent was
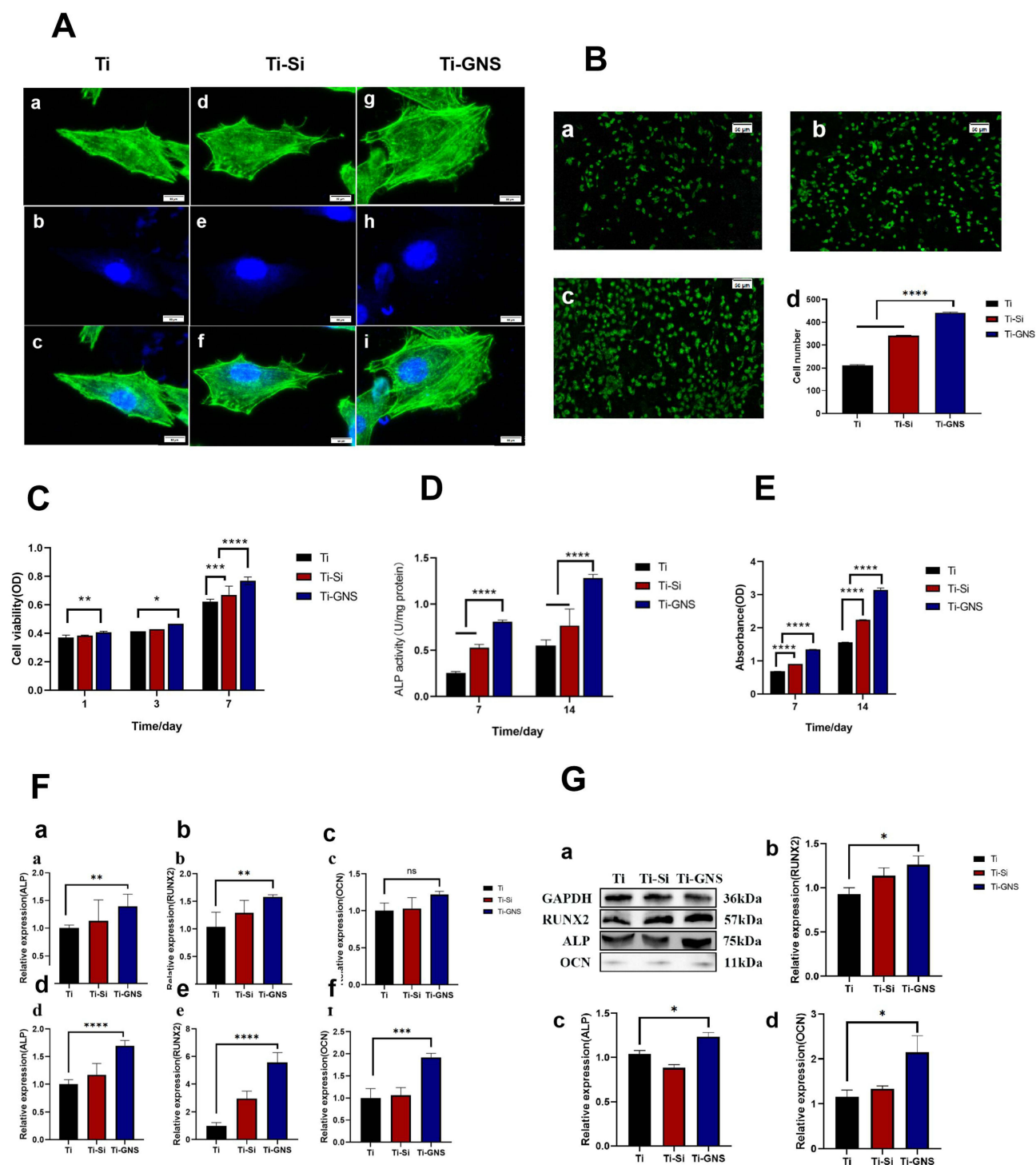
Figure 2 (**A**) Cell morphology images for the Ti group (a-c), Ti-Si group (d-f), and Ti-GNS group (g-i). Actin is stained green, and cell nuclei are stained blue. Scale bar: 20×. (**B**) Cell viability staining for the Ti group (a), Ti-Si group (b), and Ti-GNS group (c), along with a statistical chart of cell numbers (d). Scale bar: 10×. (**C**) CCK-8 assay results. (**D**) Quantitative analysis of alkaline phosphatase (ALP) activity. (**E**) Semi-quantitative analysis of cell mineralized matrix. (**F**) PCR results showing gene expression levels of ALP, RUNX2 (runt-related transcription factor 2), and OCN (osteocalcin) at 7 days (a-c) and 14 days (d-f) after osteogenic induction. (**G**) Western blot results: (a) Protein expression bands of osteogenesis-related proteins (RUNX2, ALP, OCN) across different material groups; (b) Quantitative analysis of RUNX2, (c) ALP, and (d) OCN protein expression levels. All statistical significance was determined: ns: p>0.05, *p<0.05, **p<0.01, ***p<0.001,****p<0.0001 compared to the Ti or Ti-Si group, n=5.

collected, and its OD value at a wavelength of 620 nm was measured, as depicted in Figure 2E. The results indicated that throughout the 21-day osteogenic induction period, all three groups exhibited a general increase in mineralized matrix formation. Notably, the Ti-GNS group demonstrated a significantly higher level of mineralized matrix production

compared to the other two groups, with statistically significant differences, suggesting that the Ti-GNS group effectively promotes mineralized matrix formation.

qPCR

Through the above semi-quantitative analysis of alkaline phosphatase (ALP) activity and mineralized matrix formation, the ability of Ti-GNS to promote the in vitro osteogenesis of mBMSCs was preliminarily demonstrated. To further validate these findings, the expression levels of osteogenic differentiation-related genes were examined using qRT-PCR. As illustrated in Figure 2F, the gene expression levels increased with prolonged osteogenic induction. Moreover, except for the OCN gene at 7 days, the Ti-GNS group consistently exhibited higher gene expression levels compared to the other groups, with statistically significant differences.

WB

WB experiment was conducted to further assess the expression levels of osteogenesis-related proteins. As illustrated in Figure 2G, using GAPDH as the internal control, the protein bands in the Ti-GNS group appeared slightly broader than those in the other two groups. The protein bands were then subjected to digital quantification. After 14 days of osteogenic induction, the quantified expression levels of osteogenesis-related proteins in the Ti-GNS group were significantly higher than those in the other two groups, with statistically significant differences.

In vivo Animal Test

At 4 and 8 weeks post-implantation, femoral tissues from the rats were harvested and subjected to Micro-CT analysis. NRecon software was utilized to reconstruct three-dimensional models, and the bone volume fraction (BV/TV) and trabecular number (Tb.N) values were calculated. The results are depicted in Figure 3. Panels (A) and (C) present the Micro-CT reconstructed images of the ex vivo rat tissues at 4 and 8 weeks, respectively, while panels (B) and (D) display the calculated BV/TV and Tb.N values for the implants in each group at these time points. Data analysis reveals that both the BV/TV ratio and Tb.N value increased over time across all three implant groups. Furthermore, the BV/TV ratio and Tb.N values in the Ti-GNS group were significantly higher than those in the other two groups, and the differences were statistically significant. The HE staining results in Figure 3E demonstrated notable new bone formation, with black areas indicating titanium implants and newly formed bone tissue highlighted within white boxes. At 8 weeks (d-f), all three groups exhibited increased peri-implant bone formation, reduced fibrous tissue and voids, and more organized trabecular arrangements compared to 4 weeks (a-c). The Ti-GNS group consistently displayed superior osteogenic potential at both time points, outperforming the other groups in bone induction capacity.

In vitro Antibacterial Performance Study

After culturing bacteria on the material surface for 12 hours, they were collected through ultrasonic vibration, serially diluted, and spread on plates for analysis. The results are shown in Figure 4A. Following NIR irradiation, the Ti-GNS group exhibited significant antibacterial properties, with an antibacterial rate of 97.8% against *Staphylococcus aureus* and 99.4% against *Escherichia coli*. In contrast, the other five groups showed no antibacterial activity under either dark or NIR conditions due to the absence of photosensitizers on their surfaces, and no statistically significant differences were observed in colony counts. As shown in Figure 4C, after five consecutive cycles on the same material, the antibacterial rate of the Ti-GNS group remained above 95%, confirming the stability of its antibacterial performance.

In another set of experiments, bacteria were cultured on the material surface for 12 hours, followed by fluorescent staining after 10 minutes of NIR exposure. In Figure 4B, green fluorescence indicates live bacteria, while red fluorescence represents dead bacteria. A large area of red fluorescence was observed on the surface of the Ti-GNS group, whereas the other two groups predominantly exhibited green fluorescence. This confirms the robust antibacterial properties of the Ti-GNS group, consistent with the results of previous experiments.
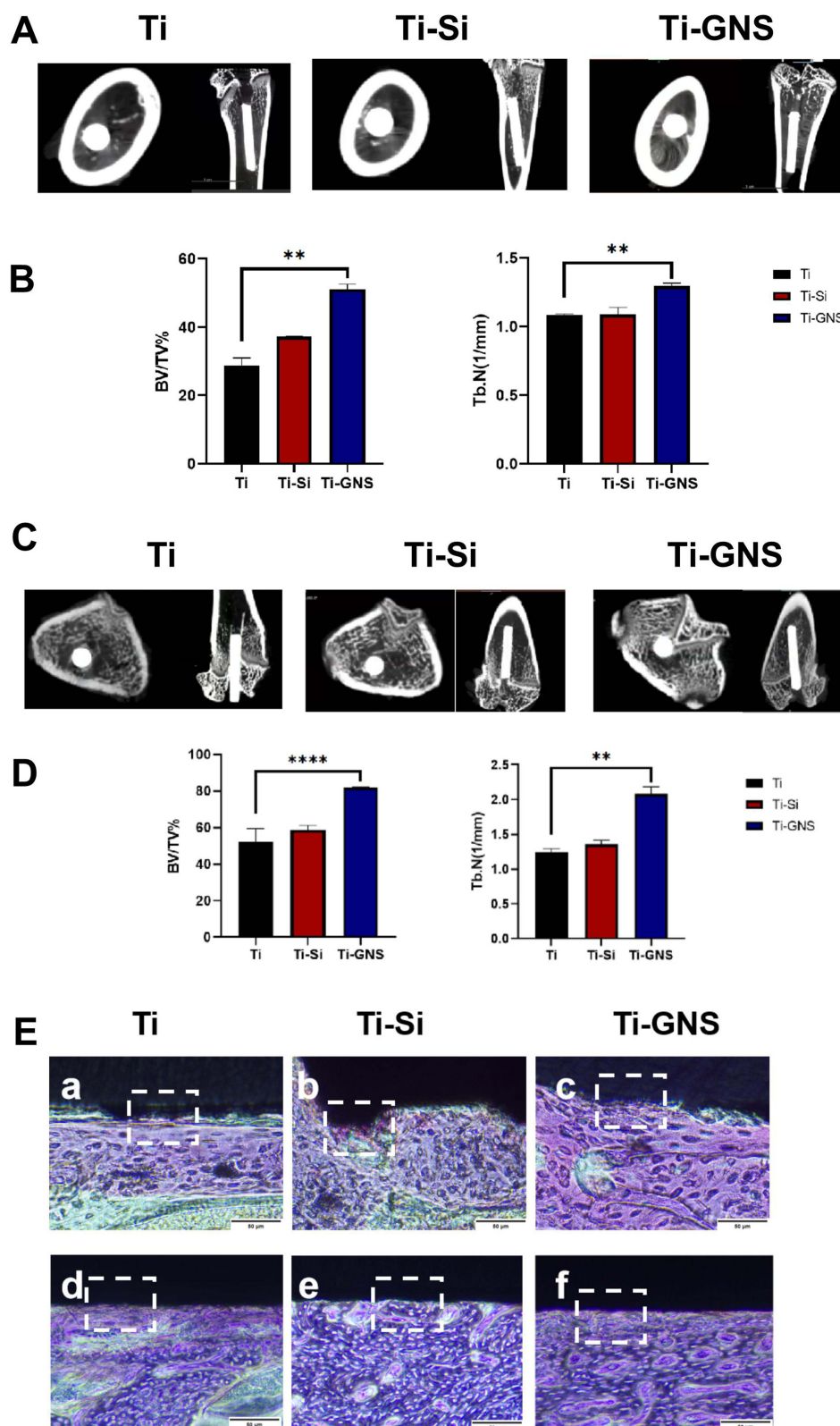
Figure 3 (**A**) Micro-CT reconstruction images at 4 weeks. (**B**) BV/TV ratio and trabecular number (Tb.N) values of implants in each group at 4 weeks. Statistical significance was determined: ** p<0.01 compared to the Ti or Ti-Si group, n=5. (**C**) Micro-CT reconstruction images at 8 weeks. (**D**) BV/TV ratio and Tb.N values of implants in each group at 8 weeks. Statistical significance was determined: **p<0.01, ****p<0.0001 compared to the Ti or Ti-Si group, n=5. (**E**) Hematoxylin and eosin (HE) staining results of hard tissue sections: 4 weeks (a-c) and 8 weeks (d-f), with newly formed bone tissue visible within the white dashed squares. Scale: 10×.

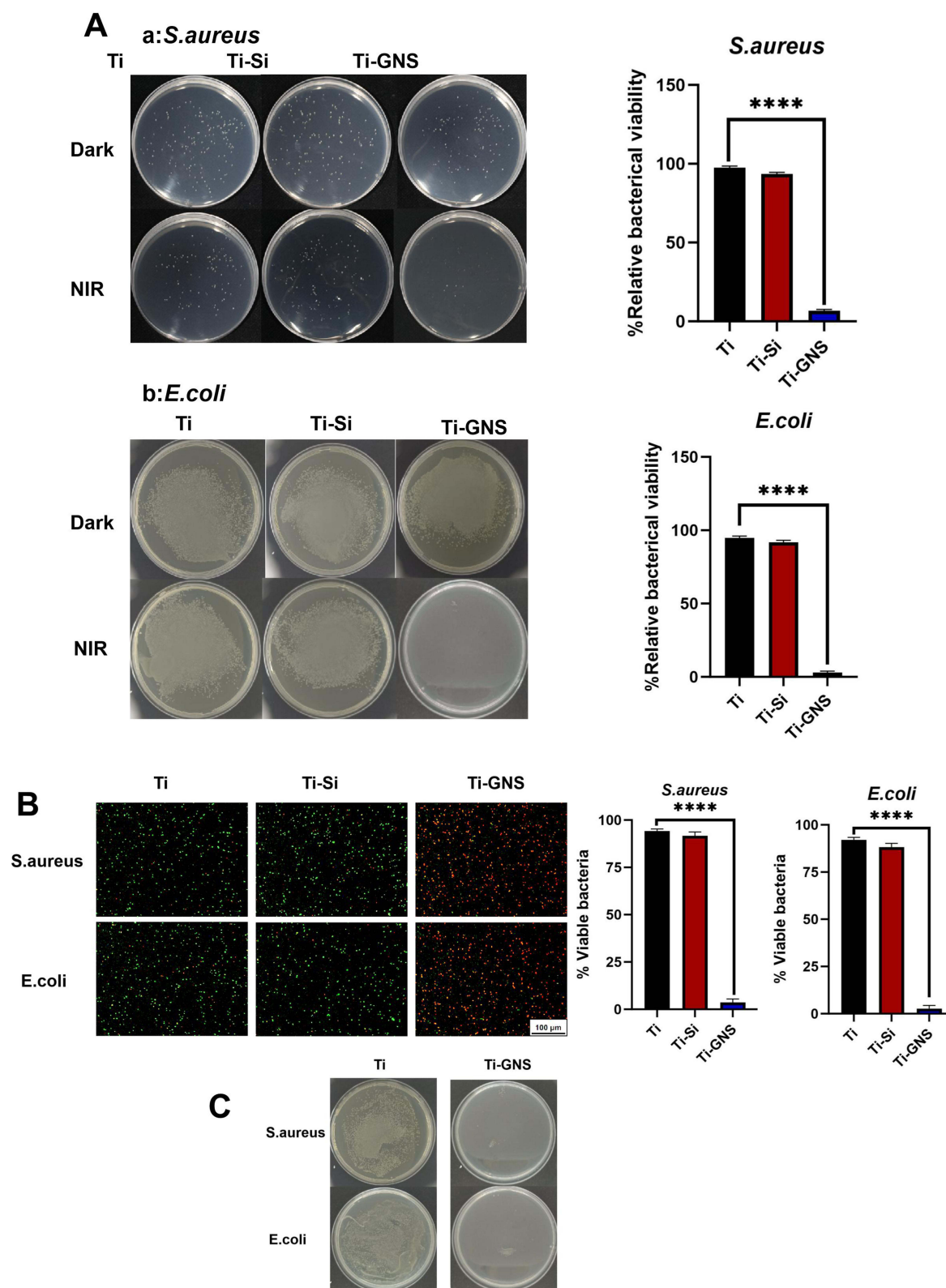**Figure 4** (**A**) Result graphs of in vitro antibacterial tests for each group: Plate-coating culture results of *Staphylococcus aureus* (a) and *Escherichia coli* (b) on the surface of each material group after incubation in darkness and under NIR irradiation. Statistical significance was determined: ****$p<0.0001$ compared to the Ti group, n=5. (**B**) Viable cell staining images: Green fluorescence indicates viable cells, while red fluorescence indicates dead cells. Scale bar: 4×.(**C**) Results of antibacterial stability tests.Statistical significance was determined: ****$p<0.0001$ compared to the Ti group, n=5.

Discussion

GNSs are star-shaped, multibranched nanoparticles with a central spherical core and outward-extending spikes of varying sizes. Various methods for synthesizing GNSs have been reported, most of which involve the chemical reduction of gold salts with the assistance of surfactants. Tuan et al observed that the morphology of the synthesized nanostars varies depending on reaction conditions such as seed concentration, temperature, and pH.[24,25] this experiment, we propose a seed- and surfactant-free synthesis method, using gold chloride solution and HEPES buffer at room temperature. This approach eliminates the need for surfactant removal and streamlines the gold nanostar preparation process, resulting in a simpler and more effective synthesis.[26,27] resulting GNSs in this study exhibited a well-dispersed distribution under low magnification in transmission electron microscopy (TEM), with no significant aggregation. At higher magnifications, the sharp, branched structures of the GNSs were clearly observed, consistent with the morphologies reported by Choo et al[26] under similar conditions. This confirms the successful synthesis of multibranched GNSs.

Once the GNSs are synthesized, deposition onto titanium surfaces must be considered. Methods for coating titanium implants with metal nanoparticle layers include electrodeposition and magnetron sputtering, in addition to chemical surface modifications. Silanization is one of the most widely used surface modification techniques, involving the treatment of metallic or non-metallic surfaces using the unique molecular structure of silanes. The chemical functional groups in silane molecules can react with hydroxyl groups on the metal surface to form covalent bonds, while also interacting with metal nanoparticles. However, since the surface of pure titanium lacks hydroxyl groups that can react with silane coupling agents, a pre-treatment is required to enable silanization. Ultraviolet-Ozone (UVO) radiation is a commonly employed surface modification method, which induces gas-phase oxidation reactions, breaking molecular chains and introducing new hydrophilic functional groups such as carboxyl and hydroxyl groups onto the titanium surface.[28–30] et al.[31] Demonstrated that UVO treatment increases hydroxyl group content on titanium surfaces, as confirmed by infrared spectral analysis. Based on this understanding, the combination of UVO and silane treatment was selected for this experiment. The titanium surface was first treated with UVO to introduce hydroxyl groups, which then reacted with the silane coupling agent MPTMS to form a silane monolayer. Subsequently, GNSs were successfully deposited onto the silanized titanium surface.

After synthesizing gold nanostar-modified titanium flakes, the microstructure of the material surface was observed using a SEM. The surface of the Ti-Si group after silanization exhibited a scale-like structure, similar to the plasma-like flakes observed on titanium flakes treated with an 8% silane reactive solution, as reported by Gully et al.[32] PS is a technique used to analyze the chemical composition and chemical states of a material's surface by detecting the energy distribution of electrons. Its core principle is based on the photoelectric effect. When a material's surface is irradiated with X-rays of sufficient energy, core electrons, known as photoelectrons, are ejected from the material. By measuring the kinetic energy of these photoelectrons, their binding energy can be calculated, enabling the determination of the elemental composition of the material's surface. EDS is an analytical technique used to detect the composition and elemental distribution of materials, with its core principle based on the generation and detection of characteristic X-rays. EDS detected the presence of Si in the Ti-Si group, although the Si content differed slightly from that reported by Zhao et al,[31] likely due to the shorter silane treatment time in this experiment—one-third of that in Zhao's study. XPS data further confirmed that Si was present in its divalent state (Si2p), suggesting the formation of Si-O-Ti covalent bonds, consistent with the principles of silanization. The successful bonding of Au nanostars was confirmed by the detection of Au in the EDS data of the Ti-GNS group and the Au4f signal in the XPS results.

Contact angle is a key indicator of a material's wettability. A contact angle greater than 90° indicates a hydrophobic surface, which resists wetting, while an angle less than 90° suggests a hydrophilic surface, which is more easily wetted. The smaller the contact angle, the greater the hydrophilicity of the material. It has been shown that the surface wettability of pure titanium materials for medical applications directly affects their biocompatibility. A smaller contact angle promotes cell adhesion and colonization, improving biocompatibility.[33] In this study, the contact angle of the pure Ti group was around 80°, indicating poor hydrophilicity. After silanization, the Ti-Si group demonstrated enhanced hydrophilicity, likely due to the formation of sulfhydryl groups on the titanium surface via MPTMS. The Ti-GNS group exhibited even higher hydrophilicity, consistent with the findings of Sobolev et al,[34] who reported that the modification of titanium surfaces with metal nanoparticles enhances hydrophilicity. AFM observations revealed that

surface roughness increased after different treatments, with the Ti-GNS group showing the greatest increase, in line with the results of Heo et al[35] for Au nanoparticle-modified titanium. This increase in surface roughness provides more sites for cell adhesion, thereby facilitating better osseointegration.[36]

GNSs have been widely used in photothermal cancer therapy and the development of photothermal antimicrobial materials due to their unique photothermal properties. The Ti and Ti-Si groups lacked photosensitizers on their surfaces for the photothermal reaction, leading to only slight temperature increases upon NIR irradiation. In contrast, the Ti-GNS group showed a rapid temperature rise, indicating that the photothermal properties of the Au nanostars were retained after deposition on the titanium surface, ensuring their continued efficacy in future photothermal applications.

Phalloidin staining was employed to fluorescently label the cell cytoskeleton, revealing normal cell morphology on the surfaces of all three material groups, with well-organized actin filaments.[37] Ti-GNS group exhibited a significant increase in pseudopodia—cellular extensions that mediate attachment to extracellular structures. This increase suggests that the Ti-GNS surface provides more binding sites for cells, indicating enhanced surface wettability and roughness, which facilitates cell adhesion and prepares cells for subsequent differentiation.[36] These findings further corroborate the material characterization results.

In live/dead cell staining, all three material surfaces displayed abundant green fluorescence with minimal red fluorescence, indicating an absence of dead cells. Under identical culture conditions, the Ti-GNS group demonstrated a stronger green fluorescence signal, confirming its superior ability to promote cell proliferation. Using the CCK-8 assay, a widely used method to assess cell proliferation, it was observed that cell proliferation increased over 1, 3, and 7 days across all groups. Statistically significant differences between the Ti-GNS and Ti groups further confirmed the biosafety of the Ti-GNS surface and its enhanced promotion of cell proliferation.

Close adhesion and rapid proliferation of cells on the implant surface are fundamental for subsequent osteogenic differentiation. To evaluate the osteogenic differentiation promoted by the Ti-GNS group, intracellular ALP activity and extracellular mineralized nodule content were measured after a period of culture in osteogenic induction medium. The results showed that the Ti-GNS group exhibited higher ALP activity and mineralized matrix content compared to the other two groups. Li et al[38] previously reported that gold nanoparticles (GNPs) with specific diameters and shapes enhance osteogenic differentiation. In this study, the star-shaped GNPs, or GNSs, demonstrated that their unique morphology did not hinder their ability to induce osteogenic differentiation.

The expression of osteogenic-related genes was analyzed using qRT-PCR. Over time, gene expression levels generally increased, and with the exception of OCN expression on day 7, the Ti-GNS group consistently showed higher levels of gene expression, with statistically significant differences compared to the other groups. Besides ALP, RUNX2 is a key marker of osteogenic differentiation, functioning as a transcription factor that initiates the differentiation process and activates the expression of other osteogenesis-related genes.[39] In this study, RUNX2 expression peaked at day 14 of osteogenic induction. While OCN expression showed no significant differences among the three groups at day 7, it increased by day 14, as OCN is a late-stage marker of osteogenic differentiation involved in extracellular matrix mineralization.[40] During the first 7 days of induction, significant mineralization had not yet occurred, consistent with the findings of Liang et al,[41] who reported that OCN expression peaks after 21 days of in vitro osteogenic induction. At both 7 and 14 days, the Ti-GNS group exhibited higher gene expression levels, confirming the promotion of osteogenic differentiation by Ti-GNS. Western blot analysis further supported these findings, showing that the Ti-GNS group had higher expression levels of key osteogenic proteins, including ALP, RUNX2, and OCN, indicating enhanced promotion of osteogenic differentiation in bone marrow mesenchymal stem cells.

The biosafety of the Ti-GNS group and its promotion of cell adhesion and proliferation were validated through cytoskeleton fluorescence staining, cell viability staining, and the CCK-8 assay. After a certain period of osteogenic induction, the Ti-GNS group demonstrated a strong ability to promote osteogenic differentiation, as confirmed by ALP activity assays, semi-quantitative analysis of extracellular mineralized matrix, PCR, and WB experiments.

For long-term stability of implants within bone tissue, achieving effective osseointegration is essential.[42] This requires the implant surface to possess adequate biocompatibility, enabling cell adhesion and colonization. However, the surface of pure titanium metal tends to form a biologically inert oxide layer. Therefore, surface modification is crucial for enhancing osseointegration.[43] By establishing an animal model, the formation of new bone around the implant can be

systematically observed over a relatively short period. In this study, SD rats were used as experimental subjects, with titanium rods implanted into both femurs to observe the integration of the implant with the surrounding bone tissue. Micro-CT imaging allows for the visualization of bone formation on and around the implant at a high resolution, enabling both qualitative and quantitative assessment of osseointegration morphology.[44] Hard tissue sectioning, which preserves the original structure and composition of bone without decalcification through a series of processes such as gradient dehydration, is the most common method for observing bone tissue. This method is particularly suitable for examining the interaction between metal implants and bone.[45] In this study, HE staining of hard tissue sections revealed that at 4 weeks, all three groups exhibited some gaps between the implants and bone, but the Ti-GNS group displayed significantly more new bone formation. By 8 weeks, the trabecular bone in all groups became more organized and compact, with reduced gaps, and the Ti-GNS group showed increased and continuous direct contact between the implant and bone tissue, indicating superior osseointegration. These findings align with the morphological observations reported by Soares et al[46] after 4 and 8 weeks, and with the Micro-CT quantitative analysis results. A comprehensive analysis of these results demonstrates that titanium implants modified with GNSs exhibit good biocompatibility and enhance osseointegration.

A major challenge for implant stability and success is bacterial infection around the implant. Although strict aseptic techniques are used during surgery, the oral cavity is a non-sterile environment, posing a significant infection risk.[47] The implant, as a foreign object, can also negatively impact the immune system. Current titanium implants lack intrinsic antibacterial properties, and studies have shown that certain bacterial species rapidly colonize the implant surface post-surgery. Once colonized, especially by *Staphylococcus aureus*, bacteria can facilitate the adhesion of other microbial species, accelerating biofilm maturation and significantly increasing the risk of peri-implantitis.[42] In the first part of this study, we successfully prepared gold nanostar-modified titanium slices, and the results confirmed their photothermal properties, providing a basis for the photothermal antibacterial experiments. Following NIR irradiation, the Ti-GNS group demonstrated significant antibacterial activity, with a 97.8% reduction in *S. aureus* and a 99.4% reduction in *E. coli*. The other five groups, which lacked photosensitizers, showed no antibacterial effects under either dark or NIR conditions. The Ti-GNS group exhibited a large area of red fluorescence, indicative of bacterial death, whereas the other groups showed predominantly green fluorescence, suggesting limited antibacterial activity. These findings were consistent with the plate coating experiment results. Moreover, after five repeated experiments, the Ti-GNS group maintained high antibacterial efficacy, indicating strong stability and reproducibility. This is attributed to the unique branched structure of GNSs, which possess two plasmon resonance peaks. Upon exposure to light of a specific wavelength, resonance occurs between the electromagnetic field of the incident light and the conduction electrons in the GNS, leading to electron oscillation. Once the light is removed, the GNS return to their ground state without any loss of their properties, ensuring the reproducibility of the photothermal effect. As the photosensitizer in this study, GNSs demonstrated excellent antibacterial performance in vitro. Based on current research findings, gold nanostar materials exhibit cytotoxicity primarily after cellular pinocytosis.[48–50] However, in our study, the gold nanostar material was immobilized on the implant surface, which significantly reduced its cellular internalization potential. Consequently, the material demonstrated minimal cytotoxicity, as evidenced by both our cell staining observations and CCK-8 assay results.

Conclusion

This study developed graphene nanosheet (GNS)-coated titanium implants (Ti-GNS), enhancing surface wettability, roughness, and photothermal activity under near-infrared (NIR) irradiation. In vitro tests confirmed Ti-GNS's biosafety and superior osteogenic performance, promoting cell adhesion, proliferation, and osteoinduction, while NIR-activated photothermal effects provided efficient antimicrobial action. However, challenges remain in ensuring long-term coating stability, optimizing clinical temperature control during photothermal therapy, and validating in vivo antimicrobial efficacy in the complex oral environment with diverse microbial communities. These findings highlight Ti-GNS's dual functionality for improving osseointegration and combating infections, though further translational research is needed.

Acknowledgments

Disclosure

The authors report no conflicts of interest in this work.

References

1. M SJC, Sordi MB, Kanazawa M, et al. Nano-scale modification of titanium implant surfaces to enhance osseointegration. *Acta Biomater*. 2019;94:112–131. doi:10.1016/j.actbio.2019.05.045

2. Wang Z, Mei L, Liu X, et al. Hierarchically hybrid biocoatings on Ti implants for enhanced antibacterial activity and osteogenesis. *Colloids Surf B Biointerfaces*. 2021;204:111802. doi:10.1016/j.colsurfb.2021.111802

3. Wang Z, Wang X, Wang Y, et al. NanoZnO-modified titanium implants for enhanced anti-bacterial activity, osteogenesis and corrosion resistance. *J Nanobiotechnology*. 2021;19(1):353. doi:10.1186/s12951-021-01099-6

4. Remísio MJDS, Borges T, Castro F, Gehrke SA, Fernandes JCH, Fernandes GVO. Histologic osseointegration level comparing titanium and zirconia dental implants: meta-analysis of preclinical studies. *Int J Oral Maxillofac Implants*. 2023;38(4):667–680. PMID: 37669522. doi:10.11607/jomi.10142

5. Kim JY, Choi H, Park JH, et al. Effects of anti-resorptive drugs on implant survival and peri-implantitis in patients with existing osseointegrated dental implants: a retrospective cohort study. *Osteoporos Int*. 2020;31(9):1749–1758. doi:10.1007/s00198-019-05257-3

6. Teixeira W, Do Nascimento C, Pereira RMA, et al. Bacterial Leakage Evaluation Through DNA-DNA Checkerboard Hybridization Technique in Morse Taper Implant-Abutment Connections: an In Vitro Study. *Int J Oral Maxillofac Implants*.2023;38:313–320.

7. Tang Y, Wang K, Wu B, et al. Photoelectrons sequentially regulate antibacterial activity and osseointegration of titanium implants. *Adv Mater*. 2024;36(2):e2307756. doi:10.1002/adma.202307756

8. Wu S, Xu J, Zou L, et al. Long-lasting renewable antibacterial porous polymeric coatings enable titanium biomaterials to prevent and treat peri-implant infection. *Nat Commun*. 2021;12(1):3303. doi:10.1038/s41467-021-23069-0

9. Song YL, Zhang SJ. Insights into peri-implantitis and its prevention][J. *Hua Xi Kou Qiang Yi Xue Za Zhi*. 2020;38(5):479–483. doi:10.7518/hxkq.2020.05.001

10. Derks J, Tomasi C. Peri-implant health and disease. A systematic review of current epidemiology. *J Clin Periodontol*. 2015;42(Suppl 16):S158–S171. doi:10.1111/jcpe.12334

11. Dohan Ehrenfest DM, Coelho PG, Kang BS, et al. Classification of osseointegrated implant surfaces: materials, chemistry and topography. *Trends Biotechnol*. 2010;28(4):198–206. doi:10.1016/j.tibtech.2009.12.003

12. de Oliveira Fernandes GV, Malta Santos NB, Correia de Sousa MF, Fernandes JCH. Liquid platelet-rich fibrin coating implant surface to enhance osseointegration: a double-blinded, randomized split-mouth trial with 1-year follow-up. *Int J Oral Maxillofac Implants*. 2022;37(1):159–170. PMID: 35235635. doi:10.11607/jomi.9107

13. Ren Y, Liu H, Liu X, et al. Photoresponsive materials for antibacterial applications. *Cell Rep Phy Sci*. 2020;1(11):100245.

14. Qiao Y, Ma F, Liu C, et al. Near-infrared laser-excited nanoparticles to eradicate multidrug-resistant bacteria and promote wound healing. *ACS Appl Mater Interfaces*. 2018;10(1):193–206.

15. Toci G, Olgiati F, Pallavicini P, et al. Gold nanostars embedded in pdms films: a photothermal material for antibacterial applications. *Nanomaterials*. 2021;11(12):3252. doi:10.3390/nano11123252

16. Chen Y, Gao Y, Chen Y, et al. Nanomaterials-based photothermal therapy and its potentials in antibacterial treatment. *J Control Release*. 2020;328:251–262. doi:10.1016/j.jconrel.2020.08.055

17. Ren Y, Yan Y, Qi H. Photothermal conversion and transfer in photothermal therapy: from macroscale to nanoscale. *Adv Colloid Interface Sci*. 2022;308:102753.

18. Li X, Lovell JF, Yoon J, et al. Clinical development and potential of photothermal and photodynamic therapies for cancer. *Nat Rev Clin Oncol*. 2020;17(11):657–674.

19. Mousavi SM, Zarei M, Hashemi SA, et al. Gold nanostars-diagnosis, bioimaging and biomedical applications. *Drug Metab Rev*. 2020;52(2):299–318.

20. Zhang D, Liu D, Zhang J, et al. Gold nanoparticles stimulate differentiation and mineralization of primary osteoblasts through the ERK/MAPK signaling pathway. *Mater Sci Eng C Mater Biol Appl*. 2014;42:70–77. doi:10.1016/j.msec.2014.04.042

21. Choi SY, Song MS, Ryu PD, et al. Gold nanoparticles promote osteogenic differentiation in human adipose-derived mesenchymal stem cells through the Wnt/β-catenin signaling pathway. *Int J Nanomed*. 2015;10:4383–4392. doi:10.2147/IJN.S78775

22. Zhou S, Pan Y, Zhang J, et al. Dendritic polyglycerol-conjugated gold nanostars with different densities of functional groups to regulate osteogenesis in human mesenchymal stem cells. *Nanoscale*. 2020;12(47):24006–24019.

23. Barbosa S, Agrawal A, Rodríguez-Lorenzo L, et al. Tuning size and sensing properties in colloidal gold nanostars. *Langmuir*. 2010;26(18):14943–14950. doi:10.1021/la102559e

24. Khoury CG, Vo-Dinh T. Gold nanostars for surface-enhanced raman scattering: synthesis, characterization and optimization. *J Phys Chem C Nanomater Interfaces*. 2008;2008(112):18849–18859. doi:10.1021/jp8054747

25. Choo P, Arenas-Esteban D, Jung I, et al. Investigating reaction intermediates during the seedless growth of gold nanostars using electron tomography. *ACS Nano*. 2022;16(3):4408–4414. doi:10.1021/acsnano.1c10669

26. Xie J, Lee JY, Wang DIC. Seedless, surfactantless, high-yield synthesis of branched gold nanocrystals in HEPES buffer solution. *Chem Mater*. 2007;19(11):2823–2830. doi:10.1021/cm0700100

27. Danyuo Y, Obayemi JD, Salifu AA, et al. Cell-surface interactions on gold-coated polydimethylsiloxane nanocomposite structures: localized laser heating on cell viability. *J Biomed Mater Res A*. 2021;109(12):2611–2624. doi:10.1002/jbm.a.37254

28. Harmankaya N, Igawa K, Stenlund P, et al. Healing of complement activating ti implants compared with non-activating ti in rat tibia. *Acta Biomater*. 2012;8(9):3532–3540. doi:10.1016/j.actbio.2012.05.017

29. Müller KH, Motskin M, Philpott AJ, et al. The effect of particle agglomeration on the formation of a surface-connected compartment induced by hydroxyapatite nanoparticles in human monocyte-derived macrophages. *Biomaterials*. 2014;35(3):1074–1088. doi:10.1016/j.biomaterials.2013.10.041

30. Linderbäck P, Harmankaya N, Askendal A, et al. The effect of heat- or ultra violet ozone-treatment of titanium on complement deposition from human blood plasma. *Biomaterials*. 2010;31(18):4795–4801.

31. Gulbanu Y, Xu G-Q, Dilnur A, et al. Silane coupler effects on titanium surface modification and biocompatibility. *Chin J Tissue Eng Res*. 2014;18(12):1864–1869.

32. Zhao B, Ma F, He D, et al. Study on antibacterial modification of silanized silver coated titanium implants. *Indust Miner Process*. 2024;53(01):8–14.

33. Valkov AA, Kossenko A, Kossenko A, et al. Bioactive coating on ti alloy with high osseointegration and antibacterial ag nanoparticles. *ACS Appl Mater Interfaces*. 2019;11(43):39534–39544. doi:10.1021/acsami.9b13849

34. Heo DN, Ko WK, Lee HR, et al. Titanium dental implants surface-immobilized with gold nanoparticles as osteoinductive agents for rapid osseointegration. *J Colloid Interface Sci*. 2016;469:129–137. doi:10.1016/j.jcis.2016.02.022

35. Seetharaman S, Etienne-Manneville S. Cytoskeletal Crosstalk in Cell Migration. *Trends Cell Biol*. 2020;30(9):720–735.

36. Li X, Xu L, Nie H, et al. Dexamethasone-loaded β-cyclodextrin for osteogenic induction of mesenchymal stem/progenitor cells and bone regeneration. *J Biomed Mater Res A*. 2021;109(7):1125–1135.

37. Fernandes GV, Cavagis AD, Ferreira CV, et al. Osteoblast adhesion dynamics: a possible role for ROS and LMW-PTP. *J Cell Biochem*. 2014;115(6):1063–1069. PMID: 24123071. doi:10.1002/jcb.24691

38. Long F. Building strong bones: molecular regulation of the osteoblast lineage. *Nat Rev Mol Cell Biol*. 2011;13(1):27–38.

39. Frank O, Heim M, Jakob M, et al. Real-time quantitative RT-PCR analysis of human bone marrow stromal cells during osteogenic differentiation in vitro. *J Cell Biochem*. 2002;85(4):737–746. doi:10.1002/jcb.10174

40. Liang H, Xu X, Feng X, et al. Gold nanoparticles-loaded hydroxyapatite composites guide osteogenic differentiation of human mesenchymal stem cells through Wnt/β-catenin signaling pathway. *Int J Nanomed*. 2019;14(2):6151–6163. doi:10.2147/IJN.S213889

41. Stoetzel S, Malhan D, Wild U, et al. Osteocytes influence on bone matrix integrity affects biomechanical competence at bone-implant interface of bioactive-coated titanium implants in rat tibiae. *Int J Mol Sci*. 2021;23(1):374. doi:10.3390/ijms23010374

42. Wang S, Zhang M, Liu L, et al. Femtosecond laser treatment promotes the surface bioactivity and bone ingrowth of Ti(6)Al(4)V bone scaffolds. *Front Bioeng Biotechnol*. 2022;10:962483. doi:10.3389/fbioe.2022.962483

43. Rebaudi A, Koller B, Laib A, et al. Microcomputed tomographic analysis of the peri-implant bone. *Int J Periodontics Restorative Dent*. 2004;24(4):316–325.

44. Danz JC, Habegger M, Bosshardt DD, et al. Virtual tissue alignment and cutting plane definition--a new method to obtain optimal longitudinal histological sections. *J Anat*. 2014;224(2):85–94. doi:10.1111/joa.12140

45. Soares PBF, Moura CCG, Chinaglia CR, et al. Effect of titanium surface functionalization with bioactive glass on osseointegration: an experimental study in dogs. *Clin Oral Implants Res*. 2018;29(11):1120–1125. doi:10.1111/clr.13375

46. Aguayo S, Donos N, Spratt D, et al. Nanoadhesion of Staphylococcus aureus onto Titanium Implant Surfaces. *J Dent Res*. 2015;94(8):1078–1084. doi:10.1177/0022034515591485

47. Fernandes GVO, Mosley GA, Ross W, Dagher A, Martins BGDS, Fernandes JCH. Revisiting socransky's complexes: a review suggesting updated new bacterial clusters (GF-MoR Complexes) for periodontal and peri-implant diseases and conditions. *Microorganisms*. 2024;12(11):2214. PMID: 39597602; PMCID: PMC11596145. doi:10.3390/microorganisms12112214

48. Sato K, Ogawa K, Tagami T, Ozeki T. Photothermal therapeutic effect by gold nanostars/extracellular vesicles nanocomplex on melanoma cells. *J Pharm Sci*. 2025;114(2):1391–1397. PMID: 39694268. doi:10.1016/j.xphs.2024.12.014

49. Wu H, Tang L, Dong H, et al. Shape and size dependence of pharmacokinetics, biodistribution, and toxicity of gold nanoparticles. *Mol Pharm*. 2025;22(1):196–208. PMID: 39589203. doi:10.1021/acs.molpharmaceut.4c00832

50. Pearl WG, Perevedentseva EV, Karmenyan AV, et al. Multifunctional plasmonic gold nanostars for cancer diagnostic and therapeutic applications. *J Biophotonics*. 2022;15(3):e202100264. PMID: 34784104. doi:10.1002/jbio.202100264